ADVANCED FUNCTIONAL MATERIALS
www.afm-journal.de



# Controllable Fabrication of Transparent Macroporous Graphene Thin Films and Versatile Applications as a Conducting Platform

*Jinhua Sun, Mushtaque A. Memon, Wei Bai, Linhong Xiao, Bin Zhang, Yongdong Jin, Yong Huang, and Jianxin Geng**

**Graphene sheets have been demonstrated to be the building blocks for various assembly structures, which eventually determine the macroscopic properties of graphene materials. As a new assembly structure, transparent macroporous graphene thin films (MGTFs) are not readily prepared due to the restacking tendency of graphene sheets during processing. Here, an ice crystal-induced phase separation process is proposed for preparation of transparent MGTFs. The ice crystal-induced phase separation process exhibits several unique features, including efficient prevention of graphene oxide restacking, easy control on the transparency of the MGTFs, and wide applicability to substrates. It is shown that the MGTFs can be used as porous scaffold with high conductivity for electrochemical deposition of various semiconductors and rare metal nanoparticles such as CdSe, ZnO, and Pt, as well as successive deposition of different materials. Notably, the macroporous structures bestow the MGTFs and the nanoparticle-decorated MGTFs (i.e., Pt@MGTF and CdSe@MGTF) enhanced performance as electrode for oxygen reduction reaction and photoelectrochemical $H_2$ generation.**

## 1. Introduction

In recent years, graphene has been demonstrated various applications due to its unique structure and unusual characteristics such as large specific surface area (theoretical value 2630 $m^2 g^{-1}$), high electrical and thermal conductivities,[1] high mechanical strength,[2] and prominent optical and electrochemical properties.[3] However, the macroscopic properties of graphene materials are determined by the assembled structures of graphene sheets. So far, various types of graphene-assembled structures have been developed, including graphene fibers,[4] 2D compact constructs including graphene papers and films,[5] and 3D porous graphene scaffolds such as monoliths[6] and beads.[7] 2D compact graphene thin films (CGTFs) can be prepared by chemical vapor deposition (CVD),[8] vacuum filtration,[5a,b] Langmuir–Blodgett method,[5c] spin coating,[9] and layer-by-layer assembly,[10] and they have been demonstrated potential applications in photoresponse and chemical/biological sensors,[10,11] as well as transparent electrodes for flexible electronic and optoelectronic devices.[5b,12] 3D porous graphene structures can be prepared by hard template-assisted CVD,[6a] hydrothermal approach,[13] freeze–drying method,[6b] and functional polymer-assisted assembly.[7,14] And such 3D graphene structures have been widely used in electromagnetic interference shielding, catalyst carriers, and energy storage and conversion.[13–15]

As a new assembly structure of graphene, transparent macroporous graphene thin films (MGTFs) that combine the features of the 2D graphene films (being micrometers thick and transparent) and the 3D porous monoliths (having macroporous structure and large specific surface area) are destined to be promising as porous electrode materials for applications such as optoelectronics, photo/photoelectrochemical catalysis, energy storage/conversion devices, and chemical/biological sensing, where the specific surface area and/or the transparency play important roles in determining the performance of electrodes.[16] However, preparation of such transparent MGTFs is challengeable due to both scientific and technical limitations: the $\pi$–$\pi$ stacking and van der Waals force interactions between the basal planes of graphene sheets result in irreversible aggregation and restacking of the graphene sheets during processing. Recently, strategies, including nucleate boiling,[17] breath figure,[18] and electrochemical deposition of graphene oxide (GO),[15e] were proposed to assemble graphene sheets into macroporous thin films. However, the walls in the macroporous structures prepared by these methods were thick due to the restacking of GO

J. Sun, M. A. Memon, W. Bai, L. Xiao, Prof. Y. Huang, Prof. J. Geng
Technical Institute of Physics and Chemistry
Chinese Academy of Sciences
29 Zhongguancun East Road, Haidian District
Beijing 100190, China
E-mail: jianxingeng@mail.ipc.ac.cn
W. Bai, Prof. B. Zhang
Key Laboratory for Anisotropy and Texture of Materials (Ministry of Education)
Northeastern University
3-11 Wenhua Road, Shenyang 110819, P. R. China
Prof. Y. Jin
State Key Laboratory of Electroanalytical Chemistry
Changchun Institute of Applied Chemistry
Chinese Academy of Sciences
5625 Ren Min Street, Changchun 130022, P. R. China

DOI: 10.1002/adfm.201501733

sheets during the evaporation of solvents and the process of electrochemical deposition, leading to decreased pore volume and increased density of the films. Therefore, it is essential to develop a simple and effective method for building MGTFs, which overcomes the restacking of the GO sheets, in order to expand and enhance the applications of graphene materials.

Here, we introduce an ice crystal-induced phase separation process for large-area construction of macroporous GO thin films, which is followed by thermal or chemical reduction to convert the macroporous GO thin films into MGTFs. The ice crystal-induced phase separation process exhibits several unique features, including efficient prevention of GO restacking, easy control of the transparency of the MGTFs, and wide applicability to substrates. In addition, the MGTFs show valuable features in high pore volume, robust adhesion to substrates, good structural stability, high electrical conductivity, and low light reflectance, making themselves a promising platform for a wide variety of applications, including as a scaffold for electrochemical deposition of semiconductors and metal nanoparticles and as electrodes for photoelectrochemical $H_2$ generation and oxygen reduction reaction (ORR). We strongly believe that the ice crystal-induced phase separation process will be capable of serving as a versatile technique for constructing MGTFs for various applications.

## 2. Results and Discussion

### 2.1. Preparation and Characterization of the MGTFs

**Figure 1**a outlines the fabrication process that comprises 1) preparation of GO hydrogel thin films by spin coating, 2) freezing of the GO hydrogel thin films in liquid $N_2$, 3) freeze drying of the GO hydrogel thin films to obtain macroporous GO thin films, and 4) thermal/chemical reduction to convert the macroporous GO thin films to MGTFs. The oxygen-containing functional groups on the surfaces of GO sheets lock a certain amount of water to make the GO hydrogel possess a viscosity. Therefore, the thickness of the GO hydrogel thin films could be readily controlled by adjusting the concentration of the GO hydrogel and modulating the spin coating speed. The thickness of the GO hydrogel films played a decisive role in determining the pore structures, which were achieved through different growth manners of the ice crystals in the GO hydrogel films of different thicknesses (see discussion later).

Scanning electron microscopy (SEM) images were recorded in order to ascertain the effect of the spin coating speed and the concentration of the GO hydrogel on the morphology and structure of the MGTFs (**Figure 2**). In each row, the MGTFs were prepared using a same GO hydrogel (e.g., 3 mg $mL^{-1}$ for the first row) and increasing spin coating speed (i.e., 600, 900, 1200, and 1500 RPM from left to right). Figure 2a displays a macroporous film of ca. 14.7 μm thickness with micron-sized open pores. The bottom was readily seen through holes in the top-view image, and the most of holes were further recognized to be continuous from top to bottom in the side-view image (the inset of Figure 2a and Figure S1a, Supporting Information). Upon increasing the spin coating speed to 900 RPM (Figure 2b), more bottom area could be identified in the thinner film, and the macroporous structures were still remained. But with further increasing the spin coating speed up to 1200 and 1500 RPM (Figure 2c,d), the macroporous structures collapsed because individual GO sheets had to be packed parallel to the substrate in a GO hydrogel film whose thickness was smaller than the lateral size of the GO sheets.

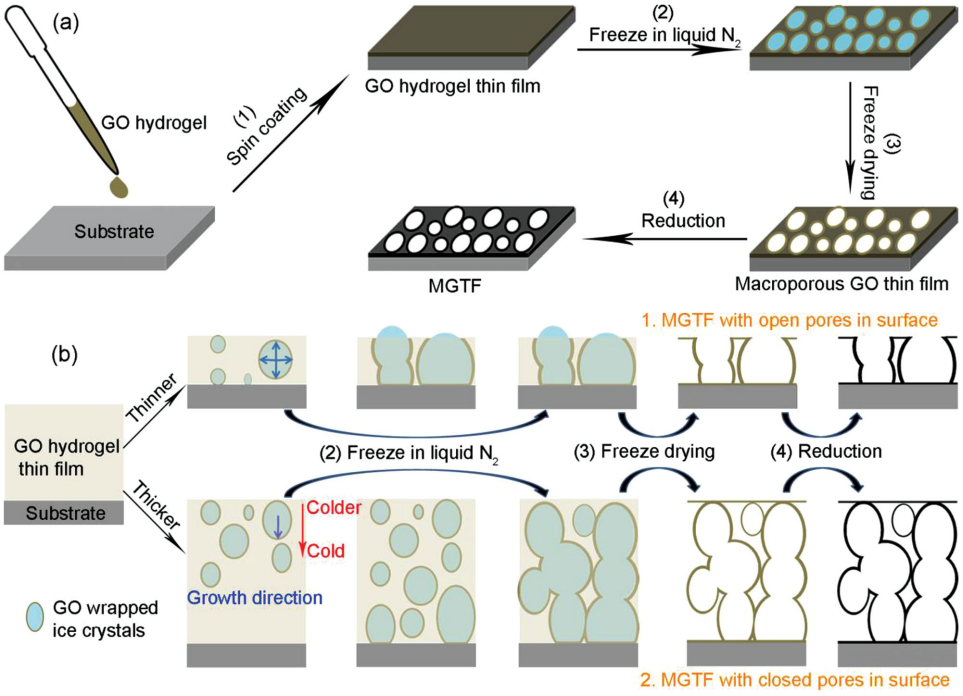


**Figure 1.** a) Preparation of the MGTFs; b) schematic illustration of the ice crystal-induced phase separation process for preparation of MGTFs. It is indicated that different types of macropores are formed in the surfaces of the MGTFs due to different thicknesses of the GO hydrogel thin films.

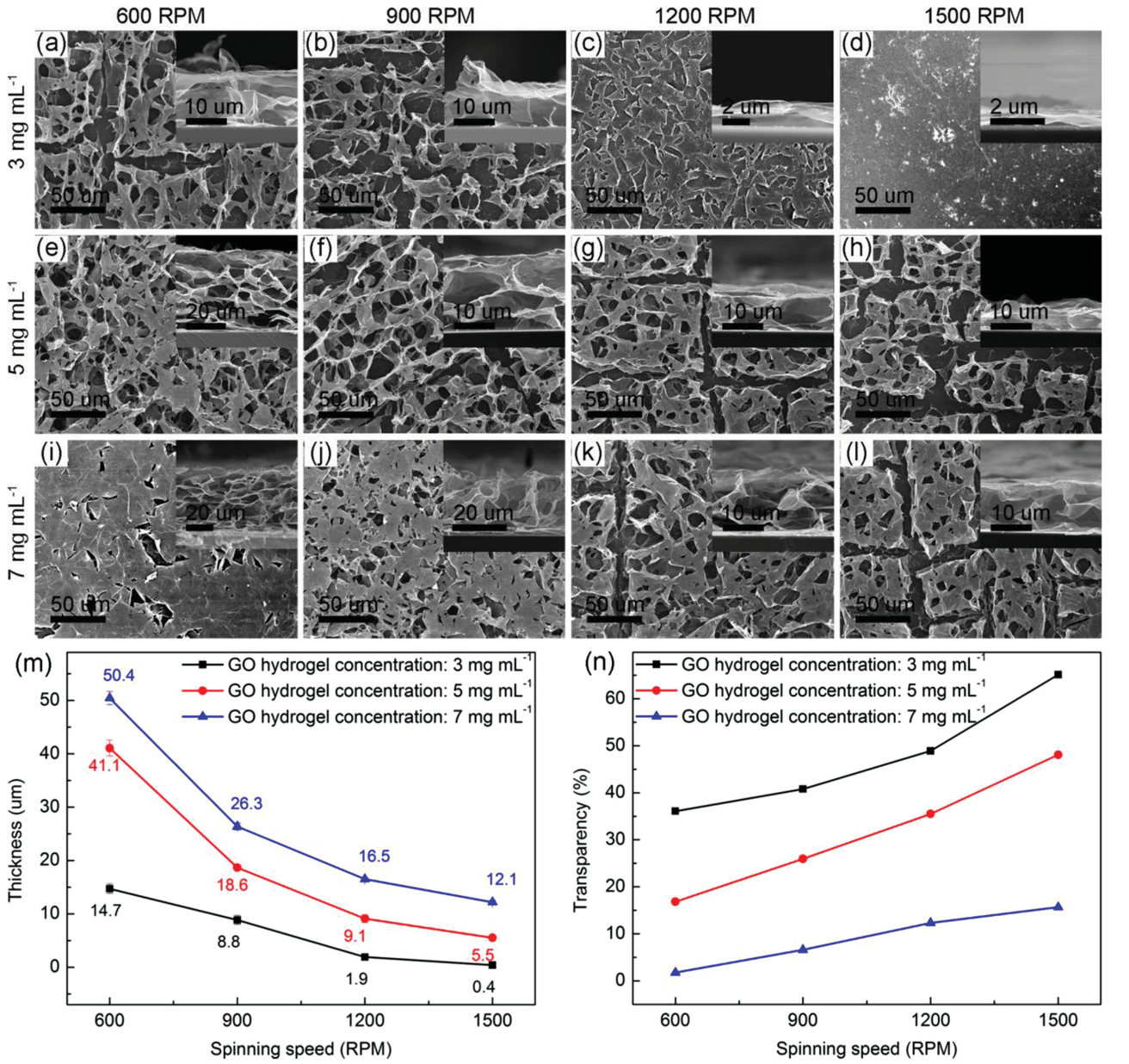


**Figure 2.** a–d) SEM images of the MGTFs fabricated from a GO hydrogel of 3 mg $mL^{-1}$ with spin coating speed of 600, 900, 1200, and 1500 RPM; e–h) SEM images of the MGTFs fabricated from a GO hydrogel of 5 mg $mL^{-1}$ with spin coating speed of 600, 900, 1200, and 1500 RPM; i–l) SEM images of the MGTFs fabricated from a GO hydrogel of 7 mg $mL^{-1}$ with spin coating speed of 600, 900, 1200, and 1500 RPM. The insets show the cross-sectional SEM images of the corresponding MGTFs. The plots of m) thickness and n) transparency of the MGTFs as function of the spin coating speed and the concentration of the GO hydrogel. These data indicate that the thickness and transparency, as well as the structure and morphology, of the MGTFs can be readily modulated by adjusting the concentration of the GO hydrogel and the spin coating speed.

In each column, the MGTFs were prepared using a same spin coating speed (e.g., 600 RPM for the first column) and increasing concentration of GO hydrogel (i.e., 3, 5, and 7 mg $mL^{-1}$ from top to bottom). Compared with the film shown in Figure 2a, a more concentrated GO hydrogel (5 mg $mL^{-1}$) yielded a thicker MGTF (Figure 2e), which contained interconnected and overlapped pores and displayed partially closed pores in the surface. With further increasing the concentration of the GO hydrogel to 7 mg $mL^{-1}$, the thickness of the MGTF was further increased (Figure 2i), and the pores in the surface became almost completely closed. By changing both the concentration of GO hydrogel and the spin coating speed, MGTFs of different thicknesses could be obtained, and these films exhibited fully open or partially open pores in the surface (Figure 2f–h,j–l). Collectively, the thickness of the MGTFs, obtained from the side-view SEM images (the insets of Figure 2 and Figure S1, Supporting Information), and the transparency of the MGTFs at 550 nm were summarized in Figure 2m,n. These results indicated

that the MGTFs was readily adjusted in the range from transparent to nontransparent by controlling the concentration of the GO hydrogel and the spin coating speed, which distinguishes our MGTFs from the 3D porous graphene block.[6] As summarized above, the surface structures of the MGTFs, i.e., having open pores or closed pores in the surfaces, were related to the thickness of the GO hydrogel films. A possible mechanism might be due to different crystallization manners of the water contained in a thinner or a thicker GO hydrogel film during the liquid $N_2$-freezing process, as outlined in Figure 1b. Upon freezing, GO sheets get accumulated between the boundaries of the ice crystals due to phase separation.[15b,19] For a thinner GO hydrogel film, the temperature gradient was negligible in the direction normal to the surface in the film so that ice crystals grew homogeneously at all directions. As a result, ice crystals were likely to protrude out of the surface of the film due to the volume expansion of water during its crystallization, leading to open pores in the surface of the MGTFs (e.g., Figure 2a). In contrast, for a thicker film, a temperature gradient was readily established in the direction normal to the surface so that ice crystals grew from the surface into the inner of the film, leading to closed pores in the surface (e.g., Figure 2i). Grooves can be seen in the MGTFs. The real time morphology evolution of the frozen GO hydrogel film during freeze drying was recorded under an environment scanning electron microscopy (ESEM) (see Movie S1, Supporting Information). It was found that the grooves were generated due to the contraction of the MGTFs during sublimation of ice. However, for the MGTFs with closed pores, the laterally packed GO sheets in the surfaces have higher strength in the lateral direction than the randomly packed GO sheets. Therefore, the size of the domains is larger in a thicker MGTF, even no grooves found in the MGTF with completely closed pores in the surface (Figure 2i).

This versatile and easily accessible solution-phase processing technique enabled the MGTFs to be readily prepared on various substrates. **Figure 3**a–c displays the uniform and large-area MGTFs prepared on regular glass (2.5 cm × 2.5 cm), ITO glass (2.5 cm × 2.5 cm), and flexible polyethylene terephthalate (PET) film (5 cm × 5 cm) using a GO hydrogel of 5 mg $mL^{-1}$ and a spin coating speed of 900 RPM. The chemical composition of the MGTFs was characterized using X-ray

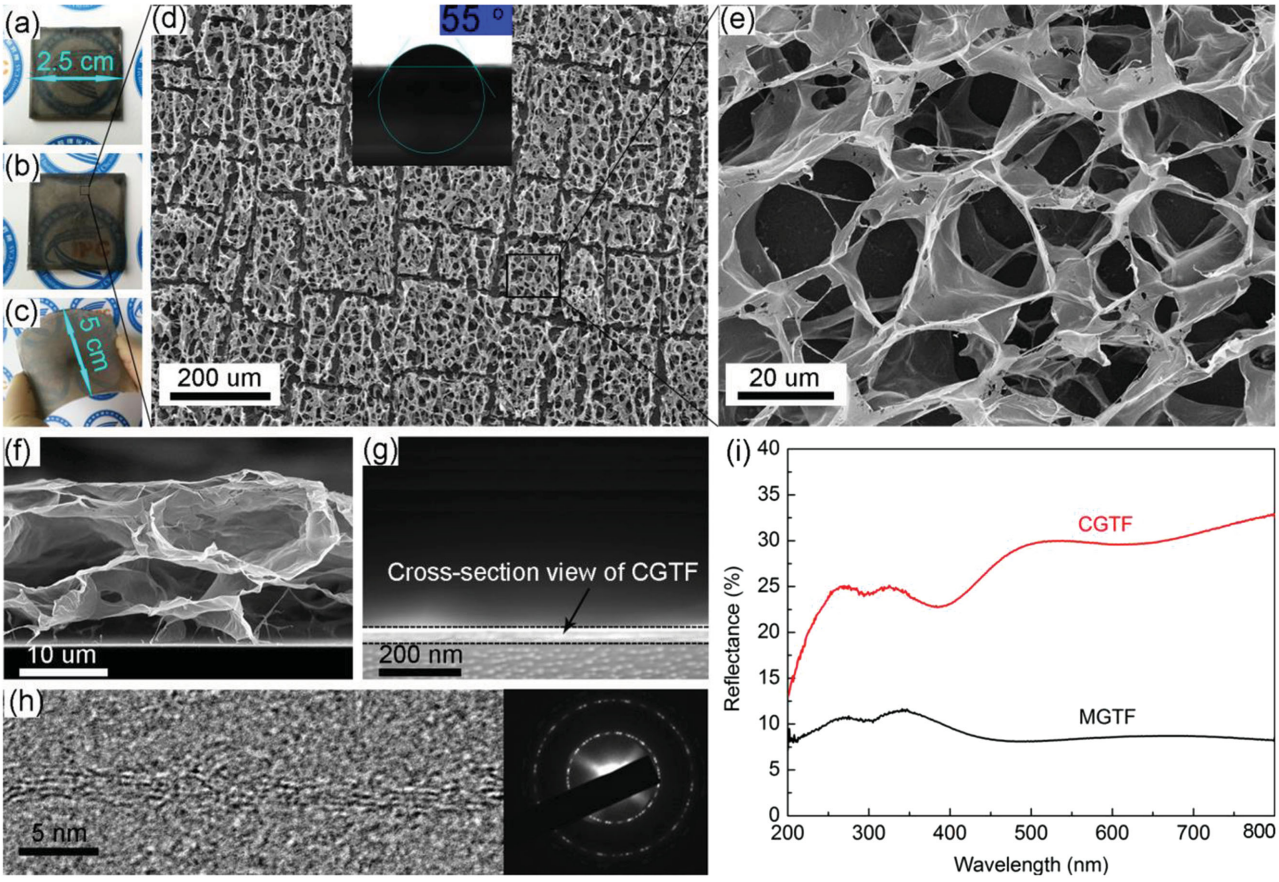


**Figure 3.** Photographs of the MGTFs prepared on a) regular glass, b) ITO glass, and c) flexible PET film. d) An SEM image of the MGTF prepared using 5 mg $mL^{-1}$ GO hydrogel at a spin coating speed of 900 RPM, with the contact angle of water on the MGTF shown in the inset. e) An SEM image of the MGTF at a higher magnification. Cross-section images of f) the MGTF and g) the CGTF. h) A HRTEM image of the MGTF recorded at the edge area of a folded RGO wall, with the corresponding ED pattern shown in the inset. i) Reflectance spectra of the MGTF and the CGTF. These data indicated that large-area MGTFs can be prepared on various substrates, and that the MGTFs have features in high specific area, hydrophilicity, and low light reflectance.

photoelectron spectroscopy (XPS) (Figure S2, Supporting Information), which indicated that the O/C atomic ratio was decreased from 0.51 for macroporous GO thin film to 0.19 for the MGTFs.[20] Figure 3d,e displays the SEM images of the MGTF prepared on ITO glass, which homogeneously show the open and interconnected macropores. Energy-dispersive X-ray spectroscopy (EDS) data indicated that the bottom seen through the pores was covered with a layer of reduced graphene oxide (RGO) (Figure S3, Supporting Information), which facilitated effective charge transportation in the MGTF, because the substrate formed the frontier for the growth of the ice crystals. The sheet resistance of the MGTF prepared on glass substrate was measured to be ca. $5.3 \times 10^4$ Ω $sq^{-1}$. Such a low sheet resistance is attributed to the thin layer of RGO covered on the substrate and the network structure of the MGTF. In addition, the MGTF showed hydrophilic feature due to the residual polar groups on the surfaces of RGO sheets (the inset of Figure 3d).[17,21] Such feature made the MGTFs be wetted well in an aqueous solution and facilitated the electrolyte diffusion in the MGTFs.[15b] Compared with a CGTF, which had a smooth surface since it was prepared by drying the GO hydrogel film naturally (Figure S4, Supporting Information), the MGTF had a larger specific surface area since it was more than 450× thicker than the CGTF (Figure 3f,g, ca. 18.6 μm for the former vs ca. 40 nm for the latter). The specific surface area of MGTFs was measured to be ca. 1.34 $m^2$ $cm^{-3}$ by the standard method of methylene blue absorption,[22] which is comparable to the value for porous graphene monolith.[23] Furthermore, high resolution-transmission electron microscopy (HRTEM) observations indicated that the walls of the MGTF were very thin, just a monolayer or a few layers of RGO sheets (Figure 3h). Electron diffraction (ED) pattern also indicated the few-layer feature of the walls (the inset of Figure 3h). The formation of thin graphene walls in the MGTFs is due to the fast crystallization of the water in the GO hydrogel films so that the irreversible aggregation and restacking of GO sheets can be suppressed. These results implied that our MGTFs have a high specific surface area compared with those prepared by breath figure method or nucleate boiling method.[17,18] Furthermore, the macroporous structure and rough morphology also affect the optical behaviors such as light reflectance of the MGTFs (Figure 3i), which is an important parameter to evaluate the light-harvesting efficiency of films. The light reflectance of the MGTF was dramatically reduced in the wavelength range of visible light (less than 8%), due to diffusive scattering of light on the macroporous surface, compared to that of the CGTF. This finding indicated that our MGTFs exhibited a higher light-harvesting efficiency than the CGTFs. For the applications associated with photo-induced charge separation such as photocatalysis and photoelectrocatalysis, the large specific surface area and low reflectance of the MGTFs would be significantly beneficial to improve the efficiency of the photophysical process due to the increased electrode/electrolyte interfaces and the enhanced light harvest (see discussion later).

### 2.2. Electrochemical Deposition of II–VI Compound Semiconductors and Rare Metal Nanoparticles into the MGTFs

Owing to their unique characteristics, i.e., thin film feature, large specific surface area, well-defined macropores, and high electrical conductivity, the MGTFs show potential application as porous electrodes. Next, we demonstrate electrochemical deposition of CdSe nanoparticles into the MGTFs. In order to create as many as possible interfaces between RGO walls and CdSe nanoparticles, the MGTFs prepared with optimized conditions (a GO hydrogel of 5 mg $mL^{-1}$, 900 RPM and 9 s for spin coating) were used as electrode for electrochemical deposition (Figure 3d). Such MGTFs not only have open pores in the surface but also have a high surface area. The open pores facilitate the easy access of reactant into the inner space of the MGTF and the high surface area guarantees high loading CdSe nanoparticles with no aggregation. **Figure 4**a displays an SEM image of CdSe@MGTF, which was prepared by electrochemical deposition of CdSe nanoparticles for 60 s. By comparing the SEM images recorded before and after electrochemical deposition (Figure 3e,4a), one can see that deposition of CdSe nanoparticles did not destroy the macroporous structure of the MGTFs. Close observation under SEM and transmittance electron microscope (TEM) revealed that the CdSe nanoparticles with diameter of ca. 30 nm were uniformly attached on the walls of the MGTFs (Figure 4b,c). The interactions between the CdSe nanoparticles and the RGO sheets were robust since the composite was subjected to sonication during sample preparation for TEM observation. HRTEM images revealed the crystalline

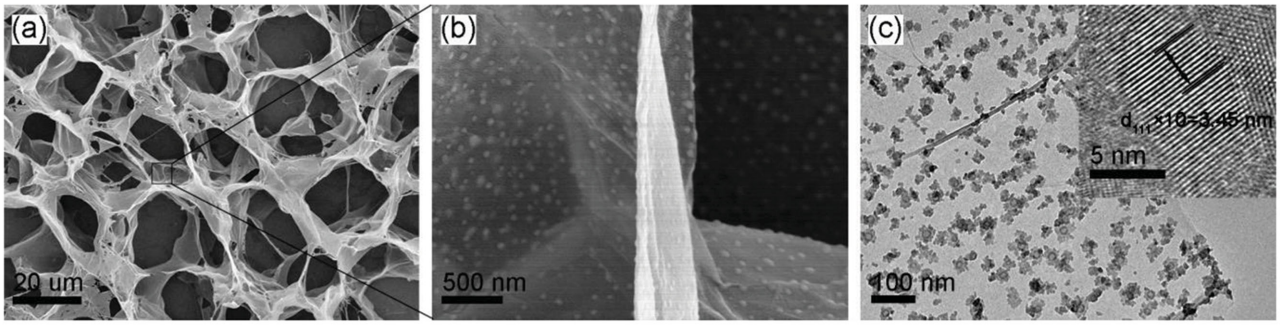


**Figure 4.** a) An SEM image of the CdSe@MGTF prepared by electrochemical deposition of CdSe nanoparticles for 60 s. b) An SEM image of the CdSe nanoparticle-decorated wall of the CdSe@MGTF recorded at a high magnification. c) A TEM image of the CdSe nanoparticle-decorated wall of the CdSe@MGTF, with the HRTEM image of a CdSe nanoparticle shown in the inset. These data indicate that CdSe nanoparticles can be uniformly deposited in the structures of the MGTFs, while the macroporous structure of the MGTFs remains intact.

feature of the CdSe nanoparticles (the inset of Figure 4c), as lattice fringes with interlayer spacing of 0.345 nm, corresponding to (111) planes, were readily observed. It was reported that CdSe nanoparticles were restricted on the edges of perfect graphene sheets in electrochemical deposition because the edge areas have a higher chemical potential than the basal planes.[24] In our study, the uniform decoration of CdSe nanoparticles could be ascribed to the residual defects throughout the RGO sheets, which acted as anchoring points to immobilize the CdSe nanoparticles.[25] In addition, the hydrophilicity of the MGTFs ensured the uniform decoration of CdSe nanoparticles on the walls throughout the macroporous structures.

The deposition of CdSe nanoparticles could be readily controlled through tuning the deposition duration. Upon increasing the deposition time, more CdSe nanoparticles were deposited, eventually to a full coverage of the RGO walls (Figure S5a,b, Supporting Information). Further elongated duration of the electrochemical deposition led to aggregation of the CdSe nanoparticles (Figure S5c–e, Supporting Information). The crystalline structure and the deposition of the CdSe nanoparticles were also investigated using X-ray diffraction (XRD) patterns and Raman spectra. The diffraction peaks at 25.4° and 42°, corresponding to (111) and (220) Bragg reflections, increased with the deposition duration (**Figure 5**a). Meanwhile, in the Raman spectra of the CdSe@MGTFs, along with the coappearance of the feature signals of RGO and CdSe nanoparticles, the Raman peaks at 205.2 and 411.1 $cm^{-1}$, corresponding to longitudinal optical (LO) and 2LO phonons of CdSe nanoparticles,[26] increased with the deposition duration (Figure 5b). These findings further supported that the deposition of CdSe nanoparticles into the MGTFs could be satisfactorily controlled.

In addition, the generality of MGTFs as electrode with high conductivity and large specific surface area for electrochemical deposition was further demonstrated by depositing other II–VI compound semiconductors and rare metal nanoparticles such as ZnO, Pt, and Pt@CdSe, which are widely applied in various areas such as catalysis, solar cells, and fuel cells.[27] SEM and XRD data indicated that the macroporous structures of the MGTFs remained intact after deposition of the aforementioned nanoparticles and that the loading quantities of those materials were also readily controlled (Figures S6–S8, Supporting Information). Significantly, the successive deposition of different materials, e.g., the fabrication of Pt@CdSe@MGTFs, demonstrated the feasibility in construction of heterojunction in the MGTFs, which would potentially expand the application of the MGTFs to ternary hybridized electrodes.

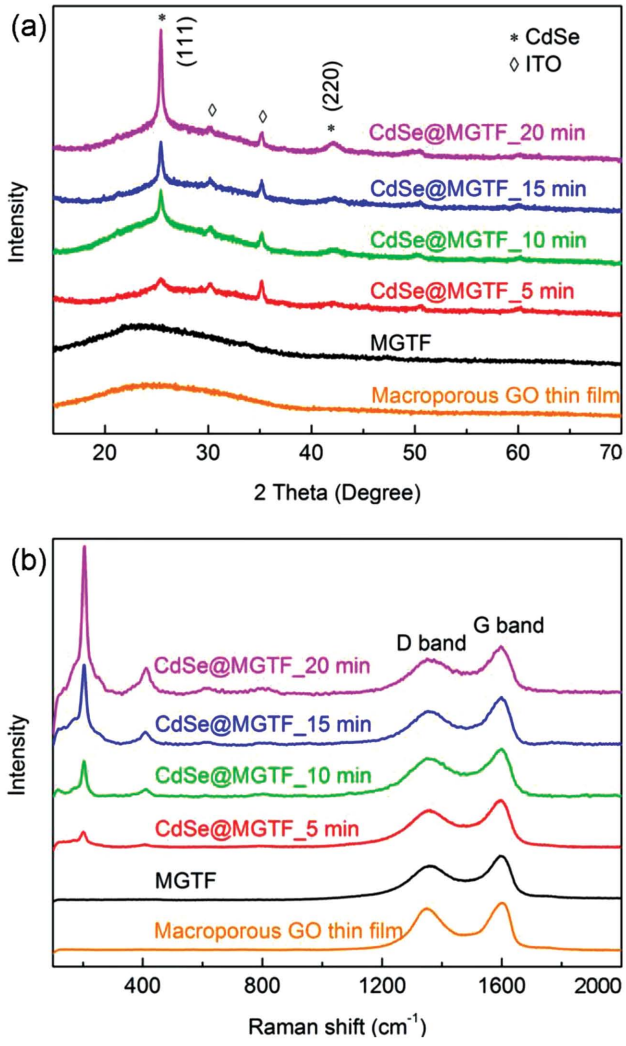


**Figure 5.** a) XRD patterns of the macroporous GO thin film, MGTF, and the CdSe@MGTFs prepared with different durations of electrochemical deposition. b) Raman spectra of the macroporous GO thin film, MGTF, and the CdSe@MGTFs prepared with different durations of electrochemical deposition. These data indicate that the deposition of CdSe nanoparticles into the MGTFs can be readily controlled through tuning the deposition duration.

### 2.3. Photoelectrochemical $H_2$ Generation Using CdSe@MGTFs

To verify the superiority of the macroporous structures of the MGTFs in the application as photoactive electrodes, the CdSe@MGTFs were used as working electrode for photoelectrochemical $H_2$ generation (**Figure 6**a). The photoelectrochemical measurements were carried out in a three-electrode cell using the CdSe@MGTF coated on a ITO substrate as working electrode, a Pt foil as counter electrode, an Ag/AgCl electrode as reference, and an aqueous solution of $Na_2S$ (0.25 M) and $Na_2SO_3$ (0.35 M) as electrolyte. In this system, the CdSe nanoparticles acted as light absorption agent, which led to optical absorption in the visible light region due to its narrow bandgap. Under illumination, the interfaces between the CdSe nanoparticles and the RGO walls resulted in efficient charge dissociation, with the photoelectrons being injected into RGO and then transported to the cathode for reduction of $H^+$. For comparison, CdSe nanoparticle-coated CGTFs (CdSe@CGTF) that had no macroporous structures were used in control tests.

Figure 6b shows the linear sweep voltammograms (LSVs) of the CdSe@MGTF and the CdSe@CGTF electrodes, which were prepared with the same duration (300 s) for electrochemical deposition of CdSe nanoparticles, in the dark and under illumination (100 mW $cm^{-2}$). In the dark, both the CdSe@MGTF and the CdSe@CGTF electrodes showed negligible currents in

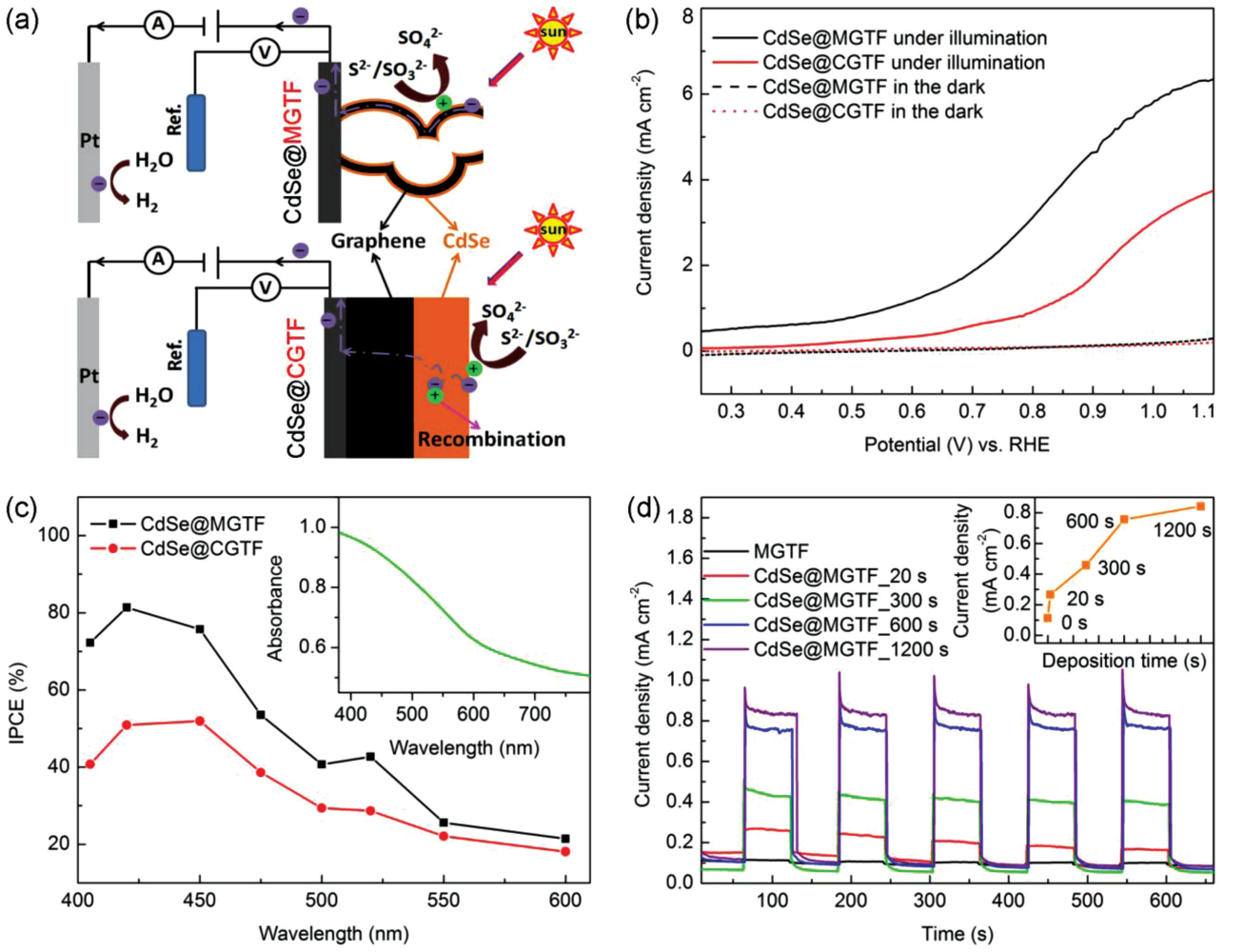


**Figure 6.** a) Schematic structures of the CdSe@MGTF and the CdSe@CGTF electrodes, which were prepared with the same parameters for the deposition of CdSe nanoparticles, for photoelectrochemical $H_2$ generation. b) The LSVs for CdSe@MGTF and CdSe@CGTF electrodes in the dark and under illumination of 100 mW cm$^{-2}$. c) IPCE spectra of the CdSe@MGTF and the CdSe@CGTF electrodes at a potential of 1 V versus the RHE, with the optical absorption spectrum of CdSe@MGTF shown in the inset. d) Amperometric *I–t* curves of MGTF electrode and the CdSe@MGTF electrodes prepared with different durations for deposition of CdSe nanoparticles at a potential of 0.6 V versus RHE as the illumination (100 mW cm$^{-2}$) was opened/chopped periodically. These data indicated that the CdSe@MGTF electrodes exhibit much enhanced performance for photoelectrochemical $H_2$ generation compared with the CdSe@CGTF electrode because the macroporous structure and the interface between RGO walls and CdSe nanoparticles facilitate light harvest and subsequent charge separation.

a potential range from 0.25 to 1.1 V versus reversible hydrogen electrode (RHE). In contrast, under illumination, although both electrodes yielded noticeable photocurrent changes at ca. 0.55 V versus RHE, the increase of the photocurrent density for the CdSe@MGTF electrode was faster than that for the CdSe@CGTF electrode and the saturated photocurrent density for the former was nearly two times higher than that for the latter (ca. 6.4 mA cm$^{-2}$ vs ca. 3.7 mA cm$^{-2}$ at 1.1 V vs RHE). These findings indicated that the recombination of the electron-hole pairs that were generated beyond the intrinsic diffusion length was avoided in the CdSe@MGTF electrode because of the uniform deposition of the CdSe nanoparticles in the macroporous structures.[28] According to Faraday's law, the loading quantities of CdSe nanoparticles on the surfaces of MGTF and CGTF were identical under the same electrochemical conditions. This suggested that the CdSe nanoparticle layer was thinner and more interfaces were formed in the CdSe@MGTF than in the CdSe@CGTF (Figures S5b and S9, Supporting Information). As a result, the photogenerated electron-hole pairs were close to the interfaces in the CdSe@MGTF, implying a short diffusion distance for the electron-hole pairs before separation (Figure 6a). In contrast, the thicker CdSe nanoparticle layer in the CdSe@CGTF electrode meant a longer diffusion distance for the photogenerated electron-hole pairs, which increased the recombination rate of electrons and holes during charge transportation.

The incident photon-to-current efficiency (IPCE) values for the CdSe@MGTF and the CdSe@CGTF electrodes were also measured at a potential of 1 V versus RHE to quantitatively evaluate the utilization efficiency of the incident light at given wavelengths (Figure 6c). Although both the CdSe@MGTF and the CdSe@CGTF electrodes exhibited the similar changing

tendency as function of wavelength, which was well-matched with the optical absorption spectrum of the CdSe@MGTF (the inset of Figure 6c), the IPCE value for the CdSe@MGTF electrode was higher than that of the CdSe@CGTF electrode at each given wavelength. The enhanced photoelectrochemical performance of the CdSe@MGTF electrode could be attributed to its macroporous structure, which exhibited favorable light harvest due to decreased light reflectance (Figure 3i) and increased interface area between the RGO sheets and the CdSe nanoparticles (Figure 4a–c). The large interface area facilitated efficient charge separation, and eventually contributed to the enhanced IPCE value for the CdSe@MGTF electrode. The superiority of the CdSe@MGTF electrode over the CdSe@CGTF electrode is attributed to the following advantages of the MGTF. First, the larger specific surface area of the MGTF than the CGTF results in more interfaces between CdSe nanoparticles and RGO walls in the CdSe@MGTF electrode; second, the lower light reflectance of the MGTFs than the CGTFs leads to higher light harvest of the CdSe@MGTF electrode; third, the RGO walls of the MGTFs serve not only as acceptor but also as electron transportation pathway, which suppresses the recombination of electrons and holes. As a result, the CdSe@MGTF electrode exhibits much enhanced performance in photoelectrochemical $H_2$ generation compared with the CdSe@CGTF electrode.

The photosensitivity of the CdSe@MGTF electrodes, defined as the percentage of enhanced current upon illumination with respect to the dark current, was further tested at a potential of 0.6 V versus RHE as the illumination (100 mW $cm^{-2}$) was opened and closed periodically. Figure S10 (Supporting Information) shows that the photosensitivity for the CdSe@MGTF electrode was ca. 9 times greater than that for the CdSe@CGTF electrode (592% for the former vs 63% for the latter). In addition, compared with other film-like electrodes derived from graphene such as graphitic carbon nitride@FTO electrode,[29] g-$C_3N_4$/N-doped graphene/$MoS_2$ ternary nanojunction,[30] $MoSe_2$-RGO/polyimide composite film,[31] and RGO-$Zn_xCd_{1-x}S$ nanocomposite,[32] the CdSe@MGTF electrode exhibits a comparable or higher photocurrent density. Finally, the influence of the quantity of CdSe nanoparticles on the photoelectrochemical performance of the CdSe@MGTF electrodes was investigated (Figure 6d). One can see that all the CdSe@MGTF electrodes, even the one prepared by deposition of CdSe nanoparticles with a very short duration (20 s), generated markedly enhanced photocurrents, compared with the MGTF electrode. The slight photoresponse of bare MGTF is attributed to the existence of bandgap structure in RGO.[33] As expected, the photocurrent increased gradually with the deposition time in the initial period (less than 600 s) (the inset of Figure 6d), indicating that the increased photocurrent was directly ascribed to the increased loading of the CdSe nanoparticles. But, upon further increasing the deposition time (to 1200 s), the corresponding CdSe@MGTF electrode did not display proportional increase in photocurrent. SEM observations indicated that a too long duration of electrochemical deposition resulted in aggregated CdSe nanoparticles, i.e., a thick CdSe nanoparticle layer. Therefore, the electron-hole pairs generated far from the interfaces would not contribute to the generation of photocurrent like the case of the CdSe@CGTF electrode. As a result, an excess of CdSe nanoparticles in the CdSe@MGTF electrode would not be beneficial to enhance the photoelectrochemical performance of the electrode.

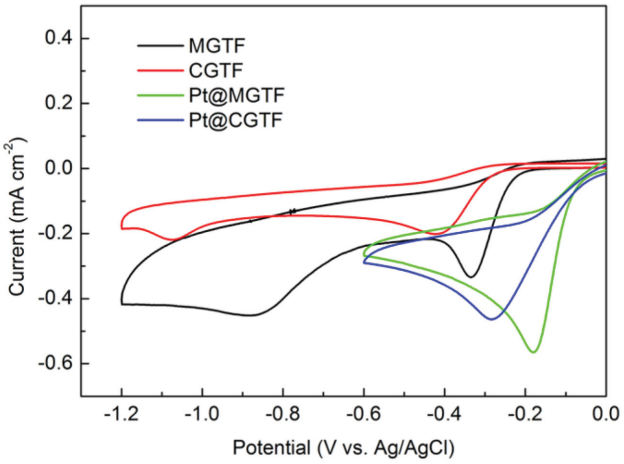


**Figure 7.** CV curves of the ORR for MGTF, CGTF, Pt@MGTF, and Pt@CGTF. These data indicate the superiority of the macroporous structure of the MGTF and the Pt@MGTF in ORR.

### 2.4. ORR of MGTF and Pt@MGTF

Recently, carbon-based catalysts were demonstrated to show improved catalytic activities in hydrogen evolution reaction,[34] oxygen evolution reaction,[35] and ORR.[36] The MGTF and Pt@MGTF electrodes were confirmed to be superior over the CGTF and Pt@CGTF electrodes in ORR due to the macroporous structures (**Figure 7**). In an $O_2$-saturated 0.1 M KOH solution, the MGTF exhibits higher ORR catalytic activity than the CGTF. This feature is reflected in the following aspects: 1) the MGTF displays a more positive onset potential for ORR than the CGTF (–0.335 V for the former and –0.422 V for the latter vs Ag/AgCl electrode); and 2) the MGTF exhibits a larger cathodic current than the CGTF. According to literatures, the catalytic activity of the MGTF for ORR is comparable to that of reported carbon-based catalysts.[37] After electrochemical deposition of Pt nanoparticles, Pt@MGTF and Pt@CGTF both exhibit enhanced catalytic activity for ORR compared with their counterparts with no Pt particles. In addition, the Pt@MGTF exhibits a more positive peak potential and a higher ORR reaction current than the Pt@CGTF electrode. This finding indicates the superiority of the macroporous structure in ORR, which could be ascribed to the facilitated reactant transport inside the pores and the increased interfaces between the catalyst and the reactant.[38] Therefore, the versatile structure features of the MGTF make itself a promising candidate for fuel cells.

## 3. Conclusion

We proposed an ice crystal-induced phase separation process for preparation of MGTFs, which overcomes the irreversible aggregation and restacking of GO sheets, leading to a high pore volume in the MGTFs. The simple solution processing method

does not need chemical modification of GO sheets, avoiding impurity involved in the MGTFs. In addition, the method also shows advantages in large-area preparation, controllable thickness, and wide suitability to substrates. Therefore, the MGTFs show potential applications as porous electrode in various areas. As a proof of concept, the MGTFs have been successfully demonstrated as scaffold for electrochemical deposition of II–VI compound semiconductors (CdSe and ZnO) and rare metal nanoparticles (Pt), as well as successive deposition of different materials (Pt@CdSe), with controllable loading quantity. And the macroporous structures facilitate to enhance the performance of the MGTF and the nanoparticle decorated electrodes (Pt@MGTF and CdSe@MGTF) in ORR and photoelectrochemical $H_2$ generation. With the valuable features aforementioned, we expect that our MGTFs will be useful as electrodes for applications in areas such as catalysis, solar cells, and energy storage and conversion.

## 4. Experimental Section

*Preparation of MGTFs*: Graphite oxide was synthesized from natural graphite powders by a modified Hummer's method.[5a,39] The graphite oxide was further purified by cycles of centrifugation and dispersion in water. The graphite oxide got exfoliated as proceeding of the purification so that the volume of the material became larger and larger. Upon exfoliation, severe centrifugation (17000 RPM and 5 h) was required to separate the GO. Such purification would not stop until the pH value of the supernatant was close to 6. After the supernatant was decanted, a GO hydrogel was obtained, as shown in Figure S11 (Supporting Information). The concentration of the as-prepared GO hydrogel was determined by drying a small portion of the hydrogel at 50 °C overnight in a vacuum oven (ca. 1.96 wt%). GO hydrogels with various concentrations (3, 5, and 7 mg $mL^{-1}$) were prepared by diluting the as-prepared GO hydrogel with DI water. Regular glass, ITO glass, and PET films were used as substrate for preparation of the MGTFs. In a typical procedure, GO hydrogel thin films were first spin coated on substrates using the aforementioned GO hydrogels at a spin coating speed of 600, 900, 1200, and 1500 RPM with the same spin coating time of 9 s. The GO hydrogel thin films were immediately frozen in liquid $N_2$ for 10 min and then transferred into a lyophilizer machine for freeze drying, leading to formation of macroporous GO thin films. Finally, the macroporous GO thin films formed on the substrates of regular glass and ITO glass were converted into MGTFs by thermal reduction at 400 °C in a tube furnace for 2 h under Ar atmosphere.[40] The macroporous GO thin films formed on PET films were converted into MGTFs by chemical reduction using hydrazine vapor at 40 °C.[33a] A series of MGTFs with different thicknesses were prepared by alternatively changing the concentration of GO hydrogel and the spin coating speed.

*Electrochemical Deposition of CdSe, ZnO, Pt, and Pt@CdSe Nanoparticles*: All the electrochemical deposition was carried out in a three-electrode electrochemical cell with the "amperometric *I–t* curve" mode using the MGTFs prepared on ITO glass as working electrode, a Pt wire as counter electrode, and an Ag/AgCl (sat. KCl) electrode as reference. CdSe nanoparticles were deposited at 55 °C using an aqueous solution containing $CdSO_4$ (0.09 M) and $SeO_2$ (0.003 M) at a potential of –0.65 V versus Ag/AgCl (sat. KCl) electrode for different durations (20–1200 s). The pH value of the solution was adjusted to be 2.5 using a $H_2SO_4$ solution. The ZnO nanoparticles were deposited at 60 °C using an aqueous solution containing $Zn(NO_3)_2$ (0.05 M) and KCl (0.05 M) at a potential of –2 V versus Ag/AgCl (sat. KCl) electrode for different durations (20–1200 s). Pt nanoparticles was deposited at room temperature using an aqueous solution containing $K_2PtCl_6$ (0.002 M) and $HClO_4$ (0.5 M) at a potential of –0.2 V versus Ag/AgCl (sat. KCl) electrode for different durations (20–1200 s). Pt@CdSe nanoparticles were deposited by successive fulfillment of the electrochemical deposition of CdSe and Pt nanoparticles using the aforementioned parameters. These nanoparticles can also be deposited on the surfaces of CGTFs by using CGTF-coated ITO substrates as working electrode.

*Photoelectrochemical $H_2$ Generation*: Photoelectrochemical $H_2$ generation was carried out in a three-electrode electrochemical cell using CdSe@MGTF or CdSe@CGTF coated on ITO glass as working electrode, a Pt foil as counter electrode, and an Ag/AgCl (sat. KCl) electrode as reference. A deaerated aqueous solution containing $Na_2S$ (0.25 M) and $Na_2SO_3$ (0.35 M) (pH ca. 12.8) was used as electrolyte. The $Na_2S$ and $Na_2SO_3$ also served as sacrificial reagent to maintain the stability of CdSe.[41] The photocurrent was recorded on a Zennium 40088 electrochemical work station under the illumination produced using a CEL-HXB UV 300 light source. The IPCE was measured under monochromatic irradiation from a Xe lamp (CEL-HXB UV 300) equipped with bandpass filters (central wavelengths: 405, 420, 450, 475, 500, 520, 550, and 600 nm; FWHM: 10 nm).

*ORR Measurement*: Cyclic voltammetry (CV) experiments (using CHI 760E) were conducted in a three-electrode electrochemical cell using a Pt foil as counter electrode, an Ag/AgCl (sat. KCl) electrode as reference, the MGTF, CGTF, Pt@MGTF or Pt@CGTF coated on ITO glass as working electrode, at a scan rate of 10 mV $s^{-1}$. Electrolyte (0.1 M KOH) was saturated with oxygen by bubbling $O_2$ for 20 min prior to the measurements.

*Characterization*: SEM observations were performed on a Hitachi S-4800 microscope operated under an accelerating voltage of 10 kV. The real time morphology evolution of a frozen GO hydrogel thin film was recorded on an ESEM (QUANTA FEG 250) as changing the vapor pressure at –20 °C. TEM images were obtained using a JEOL JEM-2100F microscope operated under an accelerating voltage of 200 kV. The XRD patterns were collected on a Bruker D8 Focus diffractometer with an incident wavelength of 0.154 nm (Cu K$\alpha$ radiation) and a Lynx-Eye detector. XPS spectra were recorded on a PHI Quantera Scanning X-ray Microprobe with a monochromated Al K$\alpha$ radiation of 1486.7 eV. Raman spectra were recorded on a Renishaw inVia Reflex confocal Raman microscope with an excitation wavelength of 532 nm. Optical absorption and transmittance spectra were recorded with a Cary 5000 spectrophotometer, and the optical reflectance spectra were collected on the same machine equipped with an integrating sphere. The contact angles were measured using the sessile drop method and recorded optically and analyzed automatically using drop shape analyzer (Contact Angle System OCA20, DataPhysics Instruments). The sheet resistance of the MGTF was measured by coating two Al contacts on the top of a MGTF with the distance between the electrodes and the length of the electrodes being equal. *I–V* curve was measured using Cryogenic Probe Station (CRX-4K, Lake Shore Cryotronics, US) and recorded by Semiconductor Parameter Analyzer (4200-SCS/F, Keithley, Tektronix, US).

## Supporting Information

Supporting Information is available from the Wiley Online Library or from the author.

## Acknowledgements

This work was supported by the "Hundred Talents Program" of Chinese Academy of Sciences and the National Natural Science Foundation of China (Grant No. U1362106).

Received: April 28, 2015
Published online: June 8, 2015

[1] a) K. S. Novoselov, A. K. Geim, S. V. Morozov, D. Jiang, Y. Zhang, S. V. Dubonos, I. V. Grigorieva, A. A. Firsov, *Science* **2004**, *306*, 666;

b) A. A. Balandin, S. Ghosh, W. Z. Bao, I. Calizo, D. Teweldebrhan, F. Miao, C. N. Lau, *Nano Lett.* **2008**, *8*, 902; c) J. B. Wu, M. Agrawal, H. A. Becerril, Z. N. Bao, Z. F. Liu, Y. S. Chen, P. Peumans, *ACS Nano* **2010**, *4*, 43.

[2] C. Lee, X. D. Wei, J. W. Kysar, J. Hone, *Science* **2008**, *321*, 385.

[3] a) R. R. Nair, P. Blake, A. N. Grigorenko, K. S. Novoselov, T. J. Booth, T. Stauber, N. M. R. Peres, A. K. Geim, *Science* **2008**, *320*, 1308; b) Y. W. Zhu, S. Murali, M. D. Stoller, K. J. Ganesh, W. W. Cai, P. J. Ferreira, A. Pirkle, R. M. Wallace, K. A. Cychosz, M. Thommes, D. Su, E. A. Stach, R. S. Ruoff, *Science* **2011**, *332*, 1537; c) H. X. Ji, X. Zhao, Z. H. Qiao, J. Jung, Y. W. Zhu, Y. L. Lu, L. L. Zhang, A. H. MacDonald, R. S. Ruoff, *Nat. Commun.* **2014**, *5*, 3317.

[4] a) Z. Xu, C. Gao, *Acc. Chem. Res.* **2014**, *47*, 1267; b) Z. Xu, C. Gao, *Nat. Commun.* **2011**, *2*, 571; c) D. S. Yu, K. Goh, H. Wang, L. Wei, W. C. Jiang, Q. Zhang, L. M. Dai, Y. Chen, *Nat. Nanotechnol.* **2014**, *9*, 555.

[5] a) J. X. Geng, H. Jung, *J. Phys. Chem. C* **2010**, *114*, 8227; b) G. Eda, G. Fanchini, M. Chhowalla, *Nat. Nanotechnol.* **2008**, *3*, 270; c) X. L. Li, G. Y. Zhang, X. D. Bai, X. M. Sun, X. R. Wang, E. Wang, H. J. Dai, *Nat. Nanotechnol.* **2008**, *3*, 538; d) J. Wang, M. H. Liang, Y. Fang, T. F. Qiu, J. Zhang, L. J. Zhi, *Adv. Mater.* **2012**, *24*, 2874.

[6] a) Z. P. Chen, W. C. Ren, L. B. Gao, B. L. Liu, S. F. Pei, H. M. Cheng, *Nat. Mater.* **2011**, *10*, 424; b) L. Qiu, J. Z. Liu, S. L. Y. Chang, Y. Z. Wu, D. Li, *Nat. Commun.* **2012**, *3*, 1241.

[7] J. L. Zou, F. Kim, *Nat. Commun.* **2014**, *5*, 5254.

[8] X. S. Li, W. W. Cai, J. H. An, S. Kim, J. Nah, D. X. Yang, R. Piner, A. Velamakanni, I. Jung, E. Tutuc, S. K. Banerjee, L. Colombo, R. S. Ruoff, *Science* **2009**, *324*, 1312.

[9] S. P. Pang, H. N. Tsao, X. L. Feng, K. Mullen, *Adv. Mater.* **2009**, *21*, 3488.

[10] J. H. Sun, L. H. Xiao, D. L. Meng, J. X. Geng, Y. Huang, *Chem. Commun.* **2013**, *49*, 5538.

[11] Y. Y. Shao, J. Wang, H. Wu, J. Liu, I. A. Aksay, Y. H. Lin, *Electroanalysis* **2010**, *22*, 1027.

[12] Y. Lee, J. Kwon, E. Hwang, C. H. Ra, W. J. Yoo, J. H. Ahn, J. H. Park, J. H. Cho, *Adv. Mater.* **2015**, *27*, 41.

[13] Z. H. Tang, S. L. Shen, J. Zhuang, X. Wang, *Angew. Chem. Int. Ed.* **2010**, *49*, 4603.

[14] W. Z. Ouyang, J. H. Sun, J. Memon, C. Wang, J. X. Geng, Y. Huang, *Carbon* **2013**, *62*, 501.

[15] a) Z. P. Chen, C. Xu, C. Q. Ma, W. C. Ren, H. M. Cheng, *Adv. Mater.* **2013**, *25*, 1296; b) S. Han, D. Q. Wu, S. Li, F. Zhang, X. L. Feng, *Adv. Mater.* **2014**, *26*, 849; c) L. M. Dai, *Acc. Chem. Res.* **2013**, *46*, 31; d) S. Krishnamurthy, P. V. Kamat, *ChemPhysChem* **2014**, *15*, 2129; e) K. X. Sheng, Y. Q. Sun, C. Li, W. J. Yuan, G. Q. Shi, *Sci. Rep.* **2012**, *2*, 247; f) J. Liang, X. Du, C. Gibson, X. W. Du, S. Z. Qiao, *Adv. Mater.* **2013**, *25*, 6226.

[16] a) H. M. Chen, C. K. Chen, Y. C. Chang, C. W. Tsai, R. S. Liu, S. F. Hu, W. S. Chang, K. H. Chen, *Angew. Chem. Int. Ed.* **2010**, *49*, 5966; b) N. Wakamatsu, H. Takamori, T. Fujigaya, N. Nakashima, *Adv. Funct. Mater.* **2009**, *19*, 311.

[17] H. S. Ahn, J. W. Jang, M. Seol, J. M. Kim, D. J. Yun, C. Park, H. Kim, D. H. Youn, J. Y. Kim, G. Park, S. C. Park, J. M. Kim, D. I. Yu, K. Yong, M. H. Kim, J. S. Lee, *Sci. Rep.* **2013**, *3*, 1396.

[18] a) S. Y. Yin, Y. Y. Zhang, J. H. Kong, C. J. Zou, C. M. Li, X. H. Lu, J. Ma, F. Y. C. Boey, X. D. Chen, *ACS Nano* **2011**, *5*, 3831; b) S. H. Lee, H. W. Kim, J. O. Hwang, W. J. Lee, J. Kwon, C. W. Bielawski, R. S. Ruoff, S. O. Kim, *Angew. Chem. Int. Ed.* **2010**, *49*, 10084.

[19] S. Deville, E. Saiz, R. K. Nalla, A. P. Tomsia, *Science* **2006**, *311*, 515.

[20] S. Chen, J. J. Duan, M. Jaroniec, S. Z. Qiao, *Adv. Mater.* **2014**, *26*, 2925.

[21] a) H. S. Ahn, H. Kim, J. M. Kim, S. C. Park, J. M. Kim, J. Kim, M. H. Kim, *Carbon* **2013**, *64*, 27; b) S. R. Wang, Y. Zhang, N. Abidi, L. Cabrales, *Langmuir* **2009**, *25*, 11078.

[22] a) J. Chen, K. X. Sheng, P. H. Luo, C. Li, G. Q. Shi, *Adv. Mater.* **2012**, *24*, 4569; b) Y. X. Xu, Z. Y. Lin, X. Zhong, X. Q. Huang, N. O. Weiss, Y. Huang, X. F. Duan, *Nat. Commun.* **2014**, *5*, 4554.

[23] Y. R. Li, J. Chen, L. Huang, C. Li, J. D. Hong, G. Q. Shi, *Adv. Mater.* **2014**, *26*, 4789.

[24] Y. T. Kim, J. H. Han, B. H. Hong, Y. U. Kwon, *Adv. Mater.* **2010**, *22*, 515.

[25] B. K. Lee, S. Y. Park, H. C. Kim, K. Cho, E. M. Vogel, M. J. Kim, R. M. Wallace, J. Y. Kim, *Appl. Phys. Lett.* **2008**, *92*, 203102.

[26] R. Venugopal, P. I. Lin, C. C. Liu, Y. T. Chen, *J. Am. Chem. Soc.* **2005**, *127*, 11262.

[27] a) K. F. Wu, Z. Y. Chen, H. J. Lv, H. M. Zhu, C. L. Hill, T. Q. Lian, *J. Am. Chem. Soc.* **2014**, *136*, 7708; b) I. Robel, V. Subramanian, M. Kuno, P. V. Kamat, *J. Am. Chem. Soc.* **2006**, *128*, 2385; c) O. H. Kim, Y. H. Cho, S. H. Kang, H. Y. Park, M. Kim, J. W. Lim, D. Y. Chung, M. J. Lee, H. Choe, Y. E. Sung, *Nat. Commun.* **2013**, *4*, 2473.

[28] Y. B. Li, T. Takata, D. Cha, K. Takanabe, T. Minegishi, J. Kubota, K. Domen, *Adv. Mater.* **2013**, *25*, 125.

[29] J. Liu, H. Q. Wang, Z. P. Chen, H. Moehwald, S. Fiechter, R. van de Krol, L. P. Wen, L. Jiang, M. Antonietti, *Adv. Mater.* **2015**, *27*, 712.

[30] Y. Hou, Z. H. Wen, S. M. Cui, X. R. Guo, J. H. Chen, *Adv. Mater.* **2013**, *25*, 6291.

[31] L. P. Jia, X. Sun, Y. M. Jiang, S. J. Yu, C. M. Wang, *Adv. Funct. Mater.* **2015**, *25*, 1814.

[32] J. Zhang, J. G. Yu, M. Jaroniec, J. R. Gong, *Nano Lett.* **2012**, *12*, 4584.

[33] a) J. H. Sun, D. L. Meng, S. D. Jiang, G. F. Wu, S. K. Yan, J. X. Geng, Y. Huang, *J. Mater. Chem.* **2012**, *22*, 18879; b) T. F. Yeh, J. M. Syu, C. Cheng, T. H. Chang, H. S. Teng, *Adv. Funct. Mater.* **2010**, *20*, 2255; c) T. T. Meng, Z. B. Zheng, K. Z. Wang, *Langmuir* **2013**, *29*, 14314.

[34] U. Sim, T. Y. Yang, J. Moon, J. An, J. Hwang, J. H. Seo, J. Lee, K. Y. Kim, J. Lee, S. Han, B. H. Hong, K. T. Nam, *Energy Environ. Sci.* **2013**, *6*, 3658.

[35] Y. Zhao, R. Nakamura, K. Kamiya, S. Nakanishi, K. Hashimoto, *Nat. Commun.* **2013**, *4*, 2390.

[36] Y. Zheng, Y. Jiao, M. Jaroniec, Y. G. Jin, S. Z. Qiao, *Small* **2012**, *8*, 3550.

[37] a) S. Y. Wang, D. S. Yu, L. M. Dai, D. W. Chang, J. B. Baek, *ACS Nano* **2011**, *5*, 6202; b) K. L. Pickrahn, S. W. Park, Y. Gorlin, H. B. R. Lee, T. F. Jaramillo, S. F. Bent, *Adv. Energy Mater.* **2012**, *2*, 1269.

[38] a) J. Liang, Y. Zheng, J. Chen, J. Liu, D. Hulicova-Jurcakova, M. Jaroniec, S. Z. Qiao, *Angew. Chem. Int. Ed.* **2012**, *51*, 3892; b) W. Wei, H. W. Liang, K. Parvez, X. D. Zhuang, X. L. Feng, K. Mullen, *Angew. Chem. Int. Ed.* **2014**, *53*, 1570.

[39] W. S. Hummers, R. E. Offeman, *J. Am. Chem. Soc.* **1958**, *80*, 1339.

[40] J. X. Geng, L. J. Liu, S. B. Yang, S. C. Youn, D. W. Kim, J. S. Lee, J. K. Choi, H. T. Jung, *J. Phys. Chem. C* **2010**, *114*, 14433.

[41] G. M. Wang, X. Y. Yang, F. Qian, J. Z. Zhang, Y. Li, *Nano Lett.* **2010**, *10*, 1088.